NANO LETTERS

2009
Vol. 9, No. 1
366-376

Exchange-Coupled Bimagnetic Cobalt/Iron Oxide Branched Nanocrystal Heterostructures

Marianna Casavola,[†,‡] Andrea Falqui,[§] Miguel Angel García,[||,⊥] Mar García-Hernández,[#] Cinzia Giannini,[▽] Roberto Cingolani,[‡,§] and P. Davide Cozzoli*[,†,‡]

Scuola Superiore ISUFI, University of Salento, Distretto Tecnologico ISUFI, via per Arnesano km 5, I-73100 Lecce, Italy, National Nanotechnology Laboratory of CNR-INFM, Unità di Ricerca IIT, via per Arnesano km 5, I-73100 Lecce, Italy, Istituto Italiano di Tecnologia, IIT, via Morego 30, I-16163 Genova, Italy, Department of Material Physics, University Complutense, E-28024 Madrid, Spain, Instituto de Ceramica y Vidrio, CSIC, C/ Kelsen 5, Campus de Cantoblanco, E-28049 Madrid, Spain, Instituto de Ciencia de Materiales de Madrid, CSIC, C/ Sor Juana Ines de la Cruz 3, Campus de Cantoblanco, E-28049 Madrid, Spain, and Istituto di Cristallografia (IC-CNR), via Amendola 122/O, I-70126 bari, Italy

Received October 17, 2008; Revised Manuscript Received November 25, 2008

ABSTRACT

A colloidal seeded-growth strategy, relying on time-programmed delivery of selected stabilizing surfactants, has been developed to synthesize bimagnetic hybrid nanocrystals (HNCs) that consist of a single-crystal tetrapod-shaped skeleton of ferrimagnetic (FiM) iron oxide functionalized with multiple polycrystalline spherical domains of ferromagnetic (FM) Co. Due to the direct bonding interfaces formed between the two materials at the relevant junction regions, the HNCs exhibit FiM-FM exchange coupling, which transcribes into a rich scenario of significantly modified properties (not otherwise achievable with any of the single components or with their physical mixtures), including higher saturation magnetization and coercitivity values, exchange biasing, and enhanced thermal stability due to induced extra anisotropy. The availability of these new types of HNCs suggests that development of appropriate synthetic tools for arranging distinct material domains in predetermined spatial arrangements could lead to a more rational design of nanoheterostructures potentially exploitable as active elements in future generations of magnetic recording devices.

The emergent demand for "smart" functional nanomaterials with enhanced technological potential is stimulating substantial efforts of colloidal nanochemistry research toward design and fabrication of complex multicomponent inorganic/organic nanostructures that can exhibit reinforced and/or tuneable chemical−physical behavior as well as multiple capabilities.[1−4] One actively pursued approach to realize this goal involves the synthesis of advanced generations of hybrid nanocrystals (HNCs), in which two or more distinct inorganic domains are assembled together through direct bonding interfaces without any molecular bridges.[1−4] Exploitation of growth mechanisms as diverse as selective heterogeneous nucleation, surface chemical activation, strain-induced phase segregation, red−ox replacement, vacancy coalescence, thermally driven oriented attachment, and intraparticle Oswald ripening has enabled proper regulation of the balance between surface and interface energies during heterostructure formation, thereby opening access to HNCs that incorporate various combinations of semiconductor, metal, and magnetic materials in controlled topologies.[3,4] Available examples include elaborate concentric or asymmetric core/shell and yolk/shell geometries, as well as intricate hetero-oligomer architectures made of shape-modulated sections interconnected via small junction areas.[3,4] In such multimaterial nanoheterostructures, control over properties and functionality is achieved through careful tailoring of the size, shape, and composition of the constituent building units, on one side, and through engineering of their relative spatial arrangement, on the other side. As a result of their inherent

* To whom all correspondence should be addressed: phone, +39 0832 298231; fax, +39 0832 298238; e-mail, davide.cozzoli@unile.it.
† Scuola Superiore ISUFI, University of Salento.
‡ National Nanotechnology Laboratory of CNR-INFM, Unità di Ricerca IIT.
§ Istituto Italiano di Tecnologia, IIT.
|| Department of Material Physics, University Complutense.
⊥ Instituto de Ceramica y Vidrio, CSIC.
Instituto de Ciencia de Materiales de Madrid, CSIC.
▽ Istituto di Cristallografia (IC-CNR).

10.1021/nl803151n CCC: $40.75
Published on Web 12/10/2008

structural complexity and of the electronic communication that is established across adjacent material portions, HNCs represent exclusive encounter platforms on which diverse optoelectronic, magnetic, and/or catalytic properties can coexist and eventually exchange-couple with each other, leading to unique nano-objects with diversified, enhanced, and/or deliberately switchable responses, not otherwise achievable with any of the individual components alone or with their physical mixture counterparts.[1−4]

All-magnetic HNCs constitute a class of functional heterostructures that have been relatively less explored, as compared to those made of associations of semiconductors and noble metals.[3−6] Major technological merits reside in the possibility to enhance the chemical robustness of a sensitive core by a protective inorganic coating, to create a surface amenable to selective organic functionalization as well as to modify the relevant magnetic features. This versatility is especially desired for optimizing performances of techniques relevant to the biomedical field, such as MRI contrast imaging, hyperthermia treatment of cancer, and magnetic sorting of targeted cells.[7,8] On the other hand, the growing efforts to reduce the ultimate dimensions of magnetic devices by use of nanostructures as the active elements come into conflict with the emergence of superparamagnetic behavior at such small domain sizes, which poses the dilemma of how thermal stability, writability, readability, and noise level, which are interdependent parameters, can be simultaneously improved at increasing integration densities.[9−18] In this regard, exploitation of magnetic coupling effects that operate through the contact boundaries between dissimilar magnetic materials promises to deliver ingenious solutions to typical limitations of nanoscale magnets.[9−28] For example, it is now being envisioned that progress in synthetic design of HNCs will ultimately allow for deliberate manipulation of exchange bias and exchange spring interactions as convenient mechanisms to induce extra anisotropy in solution-processable nanoheterostructures.[9−18] Future breeds of suitably engineered all-magnetic HNCs can thus be expected to pave the way to cost-effective bottom-up fabrication of devices for which thermal stability of magnetization is guaranteed at progressively higher levels of miniaturization.[9−28]

As a matter of fact, most advances in the development of HNCs with enhanced anisotropy and/or exhibiting unusual magnetic performances have dealt with associations of exchange-coupled antiferromagnetic (AFM) and ferro-/ferrimagnetic (FM/FiM) materials in core/shell geometries,[3,9−28] whereas examples of less conventional systems remain confined to a few prototypes of FM-FiM heterodimer architectures for which, however, cooperative magnetization switching and reduced coercitivity with no exchange biasing signature have been observed.[5,6]

Herein, we report on a straightforward colloidal seeded-growth strategy to synthesize exchange-coupled bimagnetic HNCs, individually made of a branched skeleton of FiM iron oxide to which multiple nanocrystals of FM metallic Co are directly attached. Owing to the inherent spatial development of the relevant material domains and to the numerous intimate contact heterojunctions attained, these heterostructures exhibit FiM-FM exchange coupling and induced extra anisotropy, which are manifested by higher saturation magnetization and coercitivity values, exchange bias, and enhanced thermal stability, as compared to those attainable by either their single constituents or their physical mixture counterpart.

The synthetic approach developed here combines the following key concepts (see the Supporting Information for further details): first, the use of organic-capped iron oxide nanocrystal tetrapods (TPs)[29] as foreign seed substrates onto which heterogeneous nucleation and growth of multiple secondary Co components can be selectively accomplished in noncoordinating 1-octadecene (ODE) environment; second, injection of organometallic $Co_2(CO)_8$ precursor in appropriate proportions at a controllably slow rate into a hot seed mixture (180 °C), which yields reactive monomer species necessary for the metal formation; and third, delayed delivery of excess oleic acid (OLAC) surfactant to a stage at which metal nucleation has terminated, while growth fed by continued precursor decomposition is approaching completion. The final nanocrystalline product is extracted by conventional alcohol-induced flocculation and centrifugation and thoroughly purified by repeated redispersion/precipitation cycles. The final HNCs are soluble in a variety of nonpolar solvents (e.g., chroform, toluene, hexane) due to their hydrophobic organic coating.

The representative low-magnification TEM overview in Figure 1 demonstrates the degree of synthetic control achievable in a typical seeded-growth synthesis of HNCs. The starting TP seeds (Figure 1a) are regularly sized branched nanocrystals that consist of four straight rod-shaped sections (5 ± 0.6 nm in diameter, 18 ± 2 nm in length) departing out from a central region and often terminating with tapered apexes. The tetrahedral arm arrangement can be inferred from the significantly higher contrast at the branching point for those objects which are lying on the carbon grid by means of three branches, while pointing the fourth one upward almost parallel to the electron beam. Following decomposition of the organometallic precursor at 180 °C, the formation of HNCs consisting of Co-functionalized TPs is authenticated by the observation of multiple spherical domains that closely adhere to each of the original seeds and exhibit a comparatively darker image contrast arising from the higher electron density of metallic cobalt (Figure 1b,c). These attributions are consistent with the known decomposition paths of $Co_2(CO)_8$ under inert atmosphere[19,30,31] and with our control experiments that confirmed the structural−morphological stability of the seeds under the typical synthesis conditions in the absence of the molecular cobalt source. As a general product feature, the Co domains in the HNCs decorate both the tips and the longitudinal sidewalls of the TP branches and exhibit similar dimensions regardless of the sites on which they are located (typical size variances are of the order of 10−18%). Feeding the seeds with proportionally larger $Co_2(CO)_8$ amounts allow the Co dimensions to be progressively enlarged from about ∼3 up to ∼7 nm (Figure 1b,c), beyond which further precursor

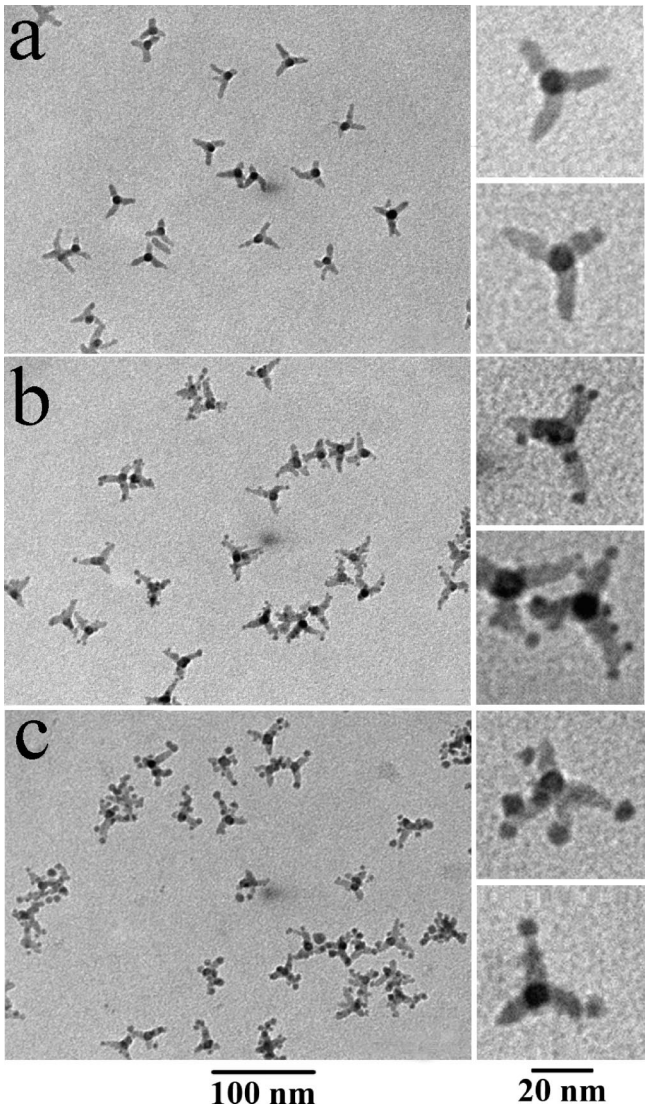

Figure 1. Representative low-resolution TEM images at different magnifications illustrating the formation of bimagnetic HNCs by a typical seeded-growth synthesis: (a) iron oxide tetrapod seeds with mean branch diameter and length of 5 ± 0.6 and 18 ± 2 nm, respectively; (b, c) Co-decorated tetrapods carrying mean Co domain dimensions of ~3 ± 0.4 and ~6 ± 0.7 nm, respectively. The initial iron oxide concentration (expressed in Fe units) was 0.04 M, while the Co:Fe reactant molar ratio was adjusted to 0.35 and 0.6 in (b) and (c), respectively.

supply leads to independent production of separated Co NCs (Figure S1 in the Supporting Information).

The attainment of HNCs with permanently connected iron oxide−Co heterojunctions is primarily corroborated by the assessment that the relative heterostructure configuration can be neither created by spontaneous assembly of TPs and free-standing Co NCs (synthesized in an independent synthesis step) upon solvent evaporation from the corresponding mixed solutions nor disrupted by any postsynthesis extraction/purification processing. An additional piece of evidence is provided by the ease with which the HNCs, which are indeed the objects with highest mass in the particle population, can be size-sorted from both unreacted TPs and separately formed Co NCs by applying conventional alcohol destabilization techniques (Figure S1 in the Supporting Information).

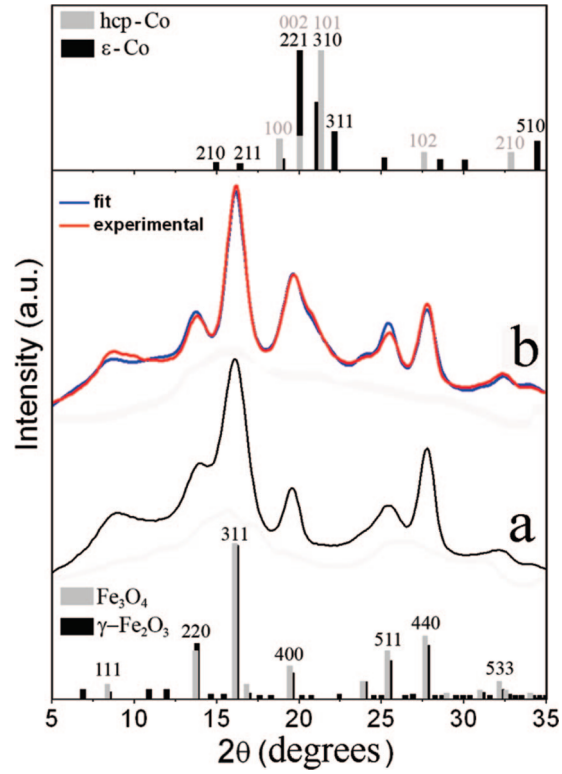

Figure 2. (a) Experimental powder XRD patterns of tetrapod seeds with mean arm diameter and length sizes of 5 ± 0.6 and 18 ± 2 nm, respectively. (b) Experimental XRD pattern (red trace) and the corresponding QPA fitting curve (blue trace) of HNCs grown from such seeds (the Co domain size is ~4.0 ± 0.6 nm, as estimated by TEM). The total Co to iron oxide weight percentage ratio calculated by QPA is estimated to be ~25% to ~75%. The reference diffraction patterns of the bulk metallic cobalt and iron oxide crystal phases are reported in the top and bottom part of the figure, respectively.

The preliminary TEM assignments have been confirmed by powder XRD investigations of the crystal-phase composition of the samples under inert atmosphere. Representative data are reported in Figure 2. The profile of the initial TP seeds (Figure 2a) can be safely indexed to the spinel cubic phases of both magnetite (Fe_3O_4) and maghemite (γ-Fe_2O_3), which cannot be discriminated because of the similarity of the respective bulk references and the significant line broadening.[32] By comparison, in the pattern of the HNCs derived from such seeds (Figure 2b, red trace) major signals of the iron oxide TPs are still recognizable, while the characteristic signature of metallic Co emerges as additional broad features in the 2θ region between ~17° and ~23°, which arise from the convolution of the spinel structure peaks with the (221), (310), and (311) reflections of the cubic ε-Co, and/or the (100), (002), and (101) reflections of hexagonal close-packed (hcp) Co, respectively. The crystal-phase composition of the samples has been further supported by quantitative phase analysis (QPA) fitting performed by an appropriate software (QUANTO) based on the Rietveld method[33] (cf. red and blue traces in Figure 2b; further details can be found in the Supporting Information). The QPA calculations highlight that the total weight fraction of the metallic Co scales up with increase in the mean size (as estimated by TEM) of the Co

domains, with the hcp-Co phase often prevailing over the ε-Co component (Figure S2 in the Supporting Information), as reported previously.[19,30,31,34] The agreement with the chemical composition deduced indirectly by inductively coupled plasma atomic emission spectroscopy (ICP-AES) measurements under the assumption that the mixtures contain only iron oxide (with equal proportions of Fe_3O_4 and γ-Fe_2O_3) and metallic cobalt is found to be within 2−4% and, hence, of the same order of the standard deviation error of the QPA fitting procedure.

The crystal structure and topological variation of the chemical composition in individual HNCs have been assessed by combining high-resolution TEM (HRTEM) investigations and energy-dispersive X-ray (EDX) elemental analyses performed in the TEM microscope operating in scanning mode (STEM). Representative results are summarized in Figure 3. The two-dimensional fast Fourier transform (2D-FFT) analyses of the HRTEM images demonstrate that the starting TP seeds (Figure 3a,b) are monocrystalline objects in the inverse spinel cubic structure of both magnetite and maghemite, which cannot be distinguished owing to the subtle differences between the respective lattice spacings. Under the observed projections, the identification of distinctive fringes, corresponding to the (3,1,1) and (0,2,−2) planes (d_{311} =2.54 Å and d_{02-2} = 2.96 Å, respectively), and the three equivalent (2,2,0), (0,−2,2), and (202) planes (d = 2.95 Å), along with the measurement of the characteristic angles among them, confirm the attributions made above. The TPs exhibit ⟨111⟩ elongated arms that often develop less straight further from the branching point and/or terminate with a more tapered profile. The darker image contrast observed in the center of the TP can be ascribed to the fourth arm protruding out of the grid plane, i.e., almost parallel to the respective zone axis direction.

Confirmation of the distribution of chemical species in the as-synthesized HNCs can be drawn from EDX spectra that have been collected in STEM mode by scanning an electron probe with a 1 nm size (which is required to achieve the necessary spatial resolution) and acquiring the characteristic X-ray fluorescence (XRF) of Fe Kα at 6.404 eV and Co Kα at 6.9303 eV (the latter overlaps with Fe Kα at 7.058 eV). The EDX spectra (right panels in Figure 3c,d) recorded from different locations of the individual HNCs that are visible in the corresponding STEM images (left panels in Figure 3c,d) show the as-acquired rough data, without taking into account the relevant cross sections of the respective atomic elements and performing any background subtraction. Despite of the long acquisition time (60−90 s), the XRF count numbers are relatively low because of the small electron probe size and of the thinness of the sampled region. Within the spatial detection limit of the EDX analysis, the examination of HNCs points out that cobalt species can be mainly found in correspondence of the spherical sections that are attached to the TPs, while iron species dominate across the branched skeleton. The detection of small contributions from Co Kα or Fe Kα associated to locations that exhibit a majority of Fe Kα or Co Kα counts, respectively, could be reasonably due to XRF from regions where the Co and the iron oxide domains partially superimpose with each other (an additional example supporting this interpretation in shown in Figure S3 of the Supporting Information). On the other hand, it is worth remarking that EDX experiments cannot distinguish between an actual atomic intermixing and the coexistence of different chemical elements in spatially segregated material domains that are simultaneously scanned by electron probe. While atomic Co diffusion through the seed is unlikely to take place to any significant extent under our mild synthesis conditions (short heating times at moderate temperature), nevertheless it cannot be excluded that the Co domains are connected to their TP substrates via an extremely thin junction region (extending over one to a few monolayers, thus not detectable by XRD) made of oxidized cobalt (Co_xO_y) and/or partially reduced iron oxide phase (possibly Fe_3O_4 or $CoFe_2O_4$) arising from interface-confined red−ox reactions.[35]

The HRTEM investigations of the HNCs are complicated by the difficulty of capturing branched heterostructures that are suitably aligned relative to the electron beam so as to exhibit lattice fringes for sections of both material components (Figure 3e−h). FFT analyses of TP branches decorated with Co either at their tips or at longitudinal sidewalls reveal that, while the iron oxide portions retain the crystal structure of the original TP seeds, the Co domains most frequently occur as polycrystalline particles. In the examples shown here, the measured spacings can be indexed to the (100), (101), (002) planes of hcp-Co (d_{100} = 2.16 Å, d_{101} = 1.91 Å, and d_{002} = 2.04 Å), in agreement with the XRD data.

We have investigated the mechanisms through which the HNCs are formed. TEM monitoring of the dimensional−morphological evolution of the reaction products reveals that the percentage of HNCs within the particle population keeps rather high and invariant over the entire synthesis course, while the Co components grow steadily over time, maintaining a relatively narrow and constant size distribution (Figure S4 in the Supporting Information). On the other hand, our control experiments highlight the reluctance of TPs to thermally coalesce with presynthesized Co NCs, which discredits any oriented crystal attachment mechanism as an alternative route by which the HNCs can be formed. Taken together, these experimental proofs indicate that the HNCs indeed originate through a temporally limited burst of heterogeneous Co nucleation onto the seeds, which is followed by the progressive enlargement of the initially formed metal nuclei over time, proportionally to the amount of organometallic precursors supplied to the reaction vessel. Our synthetic success can be rationalized within the simplified frame of the classical nucleation theory (CNT), according to which both heterogeneous nucleation of Co onto pre-existing nanocrystal seeds and subsequent autocatalytic growth indeed require overcoming a considerably lower energy barrier than that for free-standing metal clusters to be independently generated in the bulk solution.[3,4] Hence, under suitable thermal activation conditions, the seeded synthesis scheme allows homogeneous nucleation events to be circumvented, with the TP concentration regulating the relative extent of precursor consumption between heterogeneous nucleation and the growth stages.

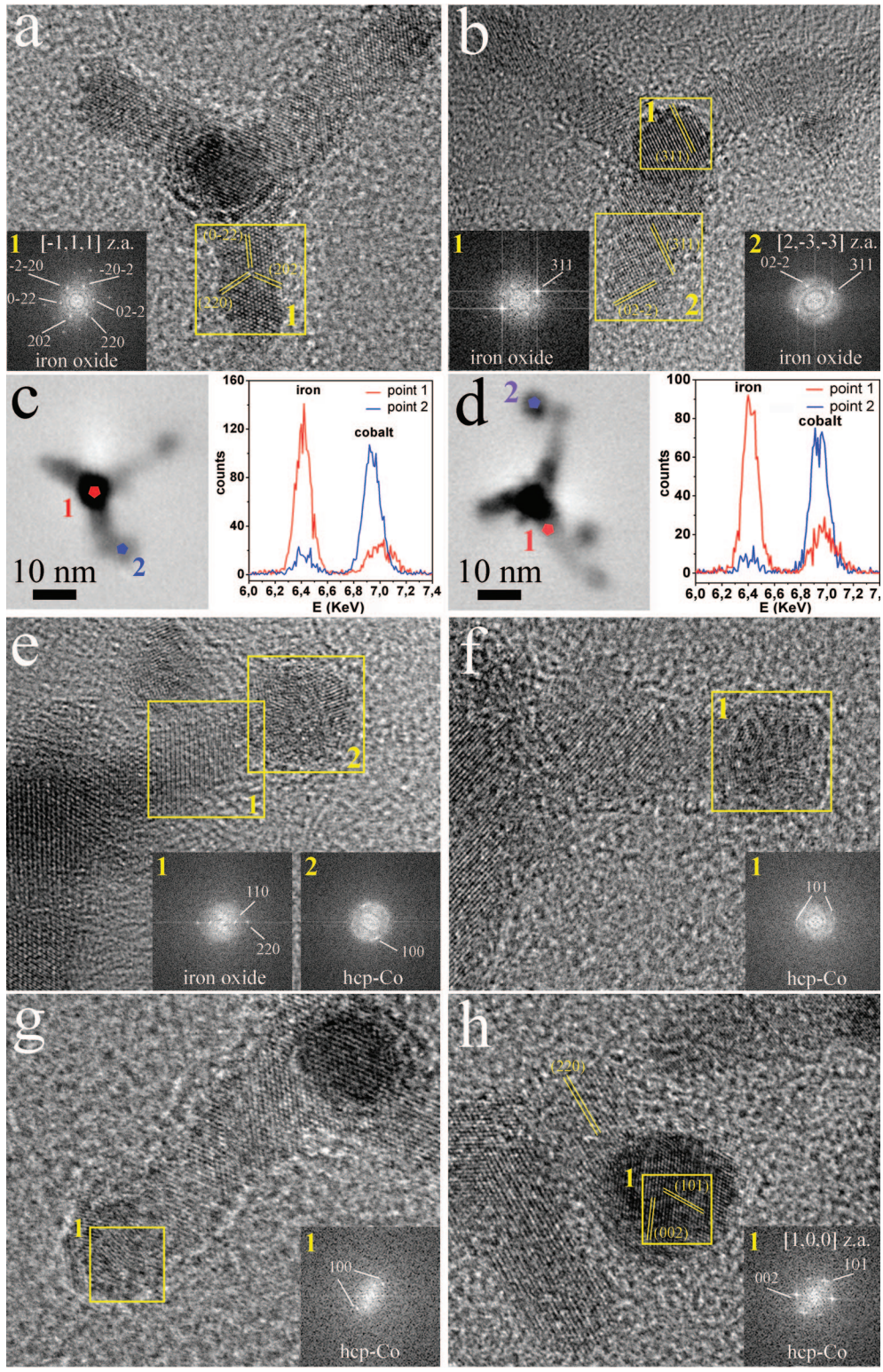

Figure 3. (a, b) Representative HRTEM images of iron oxide tetrapod seeds observed down the ⟨−1,1,1⟩ and ⟨2,−3,−3⟩ zone axes (z.a.), respectively. The yellow squares mark the regions on the nanocrystals where the 2D-FFT has been calculated and reported in the respective insets. (c, d) STEM images of individual HNCs (left panels) where the colored spots indicate the points from which the corresponding EDX spectra (right panels) were recorded. Co species are clearly dominant (blue traces in respective EDX plots) in correspondence of spherical domains attached to the tetrapod arms (regions labeled as "2" in the relevant STEM images), while Fe species (red traces in EDX plots) are prevalent across the majority of the tetrapod skeleton (e.g., in proximity of regions labeled as "1" in the respective STEM images). (e, h) Representative HRTEM images of portions of Co-decorated tetrapod HNCs observed along different zone axes. The squares indicate the regions where the FFT has been calculated and reported in the respective insets. The Co domains identified in (e−g) appear to be polycrystalline (the relevant zone axis cannot be, in fact, identified unambiguously), while the Co nanoparticle in (h) is a hcp-phase single-crystal object viewed down its ⟨1,0,0⟩ zone axis.

Such a seed-controlled synthesis dynamic ultimately accounts for the high yield with which the HNCs can be prepared.

Nevertheless, the CNT takes into account neither effects of strain fields arising from interfacial lattice mismatch at the junctions between dissimilar materials nor changes in nanostructure surface energy induced by surfactant adhesion.[1−4] The result of inducing Co deposition at a moderate temperature (180 °C) in the absence of any surfactant species suggests that the TP become chemically accessible due to the pristine capping ligands being displaced out of the surface and participating in an adsorption/desorption equilibrium between the seed and the bulk solution. Under these circumstances, any excess of reactive monomers produced by $Co_2(CO)_8$ decomposition can be efficiently depleted during extensive heterogeneous nucleation and growth of Co, which in turn inhibits independent production of separate Co NCs (Figure S5 in the Supporting Information). Therefore, the proposed synthesis technique of performing massive OLAC surfactant addition at an advanced reaction stage serves to promote and temporally restrict development of Co domains on the seeds to the initial synthesis period, as well as to guarantee completion of HNC development under aggregation-free conditions (Figure S6 in the Supporting Information). On the other hand, it is worth noting that a satisfactory degree of heterogeneous nucleation is achieved at the cost of topological selectivity, since both the number and the locations of the Co domains grown on the TPs are randomly distributed (Figure 1). Although the seed shape anisotropy may be expected to drive site-specific Co deposition (e.g., onto the apexes on the TP arms), nevertheless differences in chemical accessibility among the various crystal facets exposed should be largely attenuated in our system. In fact, because of the exceedingly low concentration of stabilizers supplied to the solution upon desorption from the seeds during the metal nucleation stage, surface-preferential ligand adhesion mechanisms could hardly operate so as to accentuate the potential facet-dependent reactivity of the TPs to any sufficient extent.[2−4,36,37] Similarly, such critically low availability of ligand species during the delicate nucleation phase as well as during the early growth period accounts for the moderately narrow size dispersion with which the decorating Co domains can be ultimately prepared.[1]

The synthesis of HNCs can be equally interpreted in terms of energy balance. The attainment of an inorganic iron oxide/Co junction can be actually regarded as a process compensating for the high surface tension that would otherwise characterize a mixture composed of separate iron oxide TPs and Co NCs in the absence of extra surface-passivating agents.[3,4,36] Hence, the creation of HNCs becomes feasible as it permits minimization of the total surface energy of a colloidal system along the organometallic precursor decomposition. The observed regime of partial Co "wetting" of the TP seed substrates, in which Co segregates in distinct domains rather than uniformly covering the TP surfaces, can be presumably ascribed to the non-negligible interfacial strain induced by lattice mismatch at the intervening junction regions between the involved materials.[1−4,36]

The magnetic performances of the newly synthesized heterostructures have been investigated by superconducting quantum interference device (SQUID) magnetometry. The impact of Co/iron oxide heterojunction formation on the resulting properties can be appreciated from the representative case of study in Figure 4, where the magnetic behavior of HNCs carrying Co domains with 5.5 nm mean size is compared with that of the bare TP seeds as well as with that of a corresponding physical mixture (MIX) made of the same TPs and unbound ∼5.5 nm Co NCs at identical Fe:Co molar ratio and similar crystal-phase composition (see Supporting Information). The relevant magnetic parameters are summarized in Table 1.

The magnetization curves at 300 K (Figure 4a) of all the samples follow a Langevin-type function showing neither remanence nor coercitivity, thus pointing to a superparamagnetic behavior. The curves recorded at low temperature after zero-field cooling (ZFC) (Figure 4b,c) reveal the specific magnetic character of the selected samples. In the case of the TP seeds (red trace in Figure 4b), the saturation magnetization at 5 K (M_S^{5K}) is of the order of 37 emu/g, hence below that for bulk cubic spinel iron oxide (around 80−85 emu/g). In spinel metal oxides, this fact is known to be correlated with the presence of a spin disordered and/or frustrated surface layer, whereby the reduced coordination number of surface atoms as well as easy axis anisotropy can favor spin configurations different from the fully aligned one.[38,39] Such a layer, featured by a spin-glasslike behavior, is known to cause a size-dependent reduction of M_S in nanostructures, like the TPs, that are indeed characterized by high surface-to-volume ratios.[29] As compared to the TP samples, the MIX sample (green curve in Figure 4b), in which the surfactant-capped iron oxide TP and Co NC components experience only weak magnetic dipolar coupling interactions,[22,38,40,41] instead shows a slightly decreased M_S^{5K} of ∼33 emu/g. Such a finding can be readily accounted for by partial mass substitution of the iron oxide material for the polycrystalline Co NC phase, the latter being characterized by somewhat lower magnetization due to concomitant surface and finite size effects as well as to the possible presence of a TEM-invisible Co_xO_y thin surface layer.[19,30,31,34,36,38,39] As for what concerns the HNCs (blue curve in Figure 4b), the first remarkable result is that their M_S^{5K} is enhanced by ∼65% relative to their MIX counterpart, which can be preliminary considered to be a genuine effect of the multiple Co/iron oxide junction interfaces that are incorporated into individual heterostructures, enabling intense coupling between the hard FM and soft FiM phases.

A comparative inspection of low-field view of the 5 K hysteresis curves (Figure 4c) discloses further distinctive properties of the HNCs relative to those of the other samples. The TPs (red trace in Figure 4c) demonstrate a complex double loop behavior marked by a characteristic kink at low fields. This suggests the presence of two decoupled phases, a softer one with coercive field $H_C \approx 60$ Oe, and a harder one with $H_C \approx 500$ Oe, which can switch almost independently. The former can be attributed to the aforementioned spin-glasslike surface phase, while the latter should reflect

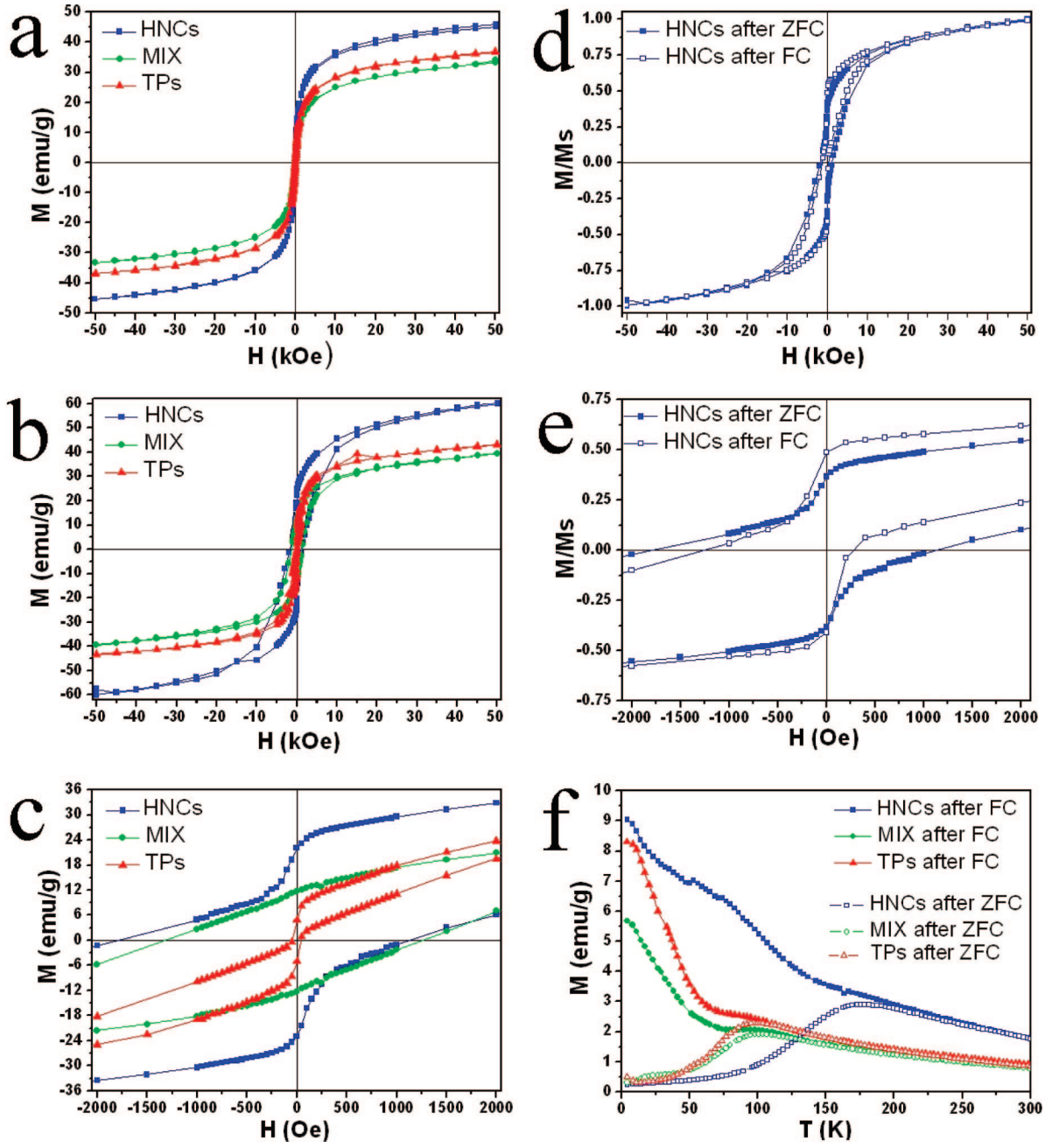

Figure 4. Comparative analysis of the magnetic properties of (i) TP seeds (with mean arm diameter and length sizes of 5 ± 0.6 and 18 ± 2 nm, respectively), (ii) thereof derived HNCs with mean Co size of 5.5 nm, and (iii) corresponding physical mixtures of the same TPs and 5.5 ± 0.7 nm Co NCs (the Co to iron oxide weight percentage composition is 32% to 68% in both cases). The magnetization values are normalized to the total sample mass. The figure panels show (a) magnetization curves at 300 K, (b, c) full and low-field expanded views of the hysteresis loops recorded at 5 K after ZFC from 300 K, respectively, (d) comparison between the normalized hysteresis loops relative to the HNC sample, which have been recorded at 5 K after FC with an applied field $H_{FC} = 5$ T and after ZFC, respectively, (e) low-field expanded view of panel d, and (f) temperature-dependent magnetization after ZFC and FC with an applied field $H_{FC} = 5$ T, respectively, measured in a 50 Oe field.

the magnetocrystalline and shape anisotropy of the ferrimagnetically ordered "core" material.[29,41,42] The fact that the curve does not become flat at saturation manifests the progressive alignment of such spin-disordered phases along the external field.[9−14] Differently, the 5 K hysteresis loop of the MIX (green trace in Figure 4c) is dominated by one hard phase with H_C as high as ∼1300 Oe, which resembles the behavior of ensembles of pure Co NCs in this size regime,[19,36] whereas the soft phase is largely depressed. This result can be understood as arising from dipolar coupling between the organic-protected FiM iron oxide and FM Co components.[22,38,40,41]

In the case of the HNCs (blue trace in Figure 4c), a pronounced change in the slope of both the ascending and descending branches of the 5K loop is visible, which discloses the coexistence of soft and hard phases with peculiar features. The soft component, whose relative contribution does not follow any clear dependence on the

Table 1. Magnetic Parameters Relative to the Samples Reported in Figure 4

	HNCs (Co size =5.5 nm)	MIX (Co size =5.5 nm)	TPs (Co absent)
M_S (emu/g)	60 ± 0.5	39 ± 0.5	43 ± 0.5
$H_{C\ (hard\ phase)}$ after ZFC (Oe)[a]	2900 ± 200	1300 ± 200	500 ± 50
$H_{C\ (hard\ phase)}$ after FC (Oe)[a]	2970 ± 200	1300 ± 200	500 ± 50
$H_{C\ (soft\ phase)}$ after FC (Oe)[a]	170 ± 20	150 ± 20	50 ± 10
$H_{C\ (soft\ phase)}$ after ZFC[a] (Oe)[a]	190 ± 20	160 ± 20	60 ± 10
$H_{EB\ (hard\ phase)}$ after FC (Oe)[a]	385 ± 20		
$H_{EB\ (hard\ phase)}$ after ZFC (Oe)[a,b]	300 ± 20		
T_B (K)	182 ± 1	100 ± 1	96 ± 1

[a] The H_C and H_{EB} values relative to the soft and hard phases have been estimated by a graphical procedure, illustrated in Figure S10 of the Supporting Information. [b] The zero-field-cooled hysteresis loop was measured after performing the field-cooled temperature-dependent magnetization measurements.

Table 2. Magnetic Parameters Relative to the Samples Reported in Figure 5

	HNCs (Co size = 3.5 ± 0.4 nm)[a]	HNCs (Co size = 5.0 ± 0.7 nm)[b]
M_S (as-prepared) (emu/g)	66 ± 0.5	62 ± 0.5
M_S (air exposed) (emu/g)	48 ± 0.5	43 ± 0.5
$H_{C(soft\ phase)}$ (air exposed) after FC (Oe)[c]	150 ± 20	170 ± 20
$H_{C(soft\ phase)}$ (as-prepared) after ZFC (Oe)[c]	165 ± 25	190 ± 25
$H_{EB(soft\ phase)}$ (air exposed) after FC (Oe)	5 ± 30	
$H_{EB(soft\ phase)}$ (as-prepared) after ZFC (Oe)[c]		
$H_{C(hard\ phase)}$ (air exposed) after FC (Oe)[c]	1300 ± 200	1950 ± 200
$H_{C(hard\ phase)}$ (as-prepared) after ZFC (Oe)[c]	2850 ± 200	3100 ± 200
$H_{EB(hard\ phase)}$ (air exposed) after FC (Oe)[c]	11 ± 40	5 ± 30
$H_{EB(hard\ phase)}$ (as-prepared) after ZFC (Oe)[c]	290 ± 20	275 ± 20
T_B (as-prepared) (K)	183 ± 1	184 ± 1
T_B (air exposed) (K)	176 ± 1	178 ± 1

[a] After oxidation, the metal Co domain core size reduced to about 60% of the original volume. [b] After oxidation, the metal Co domain core size reduced to about 40% of the original volume. [c] The H_C and H_{EB} values relative to the soft and hard phases have been estimated by a graphical procedure, illustrated in Figure S10 of the Supporting Information.

Co domain size (cf. Tables 1 and 2 and Figures S7−S9 in the Supporting Information), possesses H_C as high as ∼190 Oe, which may originate partly from the spin-glasslike surface phase of the TP skeleton and partly from the multiple Co_xO_y−$CoFe_2O_4$ interfaces at the small iron oxide/Co connecting regions.[35] The hard phase component of the HNCs generally shows a considerably enhanced H_C value of ∼2700 Oe after ZFC, which can reach up to ∼3600 Oe, depending nonmonotonically on the average Co dimensions (cf. Tables 1 and 2 and Figures S7−S9 in the Supporting Information). This experimental proof represents a further hint that the iron oxide TPs and the decorating Co domains are exchange-coupled due to the formation of direct bonding junctions. The fact that the loop of the HNCs does not reach saturation at high field values manifests the progressive alignment of the newly attained hard phase with enhanced anisotropy along the external field. On the other hand, any possible involvement of a thin AFM Co_xO_y shell on the surface of the Co domains (e.g., formed serendipitously during sample processing and/or manipulation) as the main source of extra anisotropy can be reasonably considered less relevant, since such a layer would cause similar coercitivity enhancement also in the MIX sample.[19,36]

Notably, the 5 K hysteresis loop of the HNC sample recorded after field-cooling (FC) from 300 K in the presence of a large magnetic field H_{FC} = 5 T (Figure 4d,e) is not centered about the origin and is shifted along the field axis toward negative values by an exchange bias (EB) field, H_{EB}. In particular, increases in H_{EB} and H_C up ∼390 Oe and to 2970 Oe, respectively, are most exclusively detected for the hard phase component, as compared to the corresponding values measured after the zero-field-cooling (ZFC). In contrast, the soft phase component remains practically unaffected by the FC procedure (Table 1). Both exchange-bias and coercitivity enhancement achieved after FC, the former revealing unidirectional anisotropy and the latter pointing to induced uniaxial or multiaxial anisotropy, are reminiscent of the behavior of bilayered and core/shell FM-AFM NCs[3,9−14,17,23−28] and can be preliminarily taken as the signature of exchange coupling between the FiM "core" phase of the iron oxide TPs and the FM phase of the attached Co domains.[9−14,17,23−25,43] Due to interactions across the junction interface, the harder FM metal sections will experience an extra H_{EB} field (in addition to the one applied externally) being exerted by the spins in the magnetically "softer" FiM material which become aligned parallel to the spins in the magnetically "harder" FM upon the FC procedure. The lack of any clear dependence of H_{EB} and H_C values on the Co domain size as well as the relatively moderate changes of their values after FC (cf. Tables 1−2) can reasonably be related to the rather intricate nature of the present Co−TP interfaces, whereby the competing impacts of the polycrystalline nature of Co, the varying extensions of the contact areas, interfacial roughness, and strain between the two material lattices at the randomly distributed junction sites, interplay in a complex way, ultimately smoothing out the detectable effects.[9−28] Nevertheless, the fact that EB, albeit less pronounced ($H_{EB} \approx 300$ Oe), is observed in the HNCs even after ZFC (note that the ZFC loop has been recorded after measuring the FC temperature dependent measurements, which implies the existence of residual magnetization in the sample) indicates that a substantial degree of coupling already exists in the native heterostructures, which can give rise to noticeable memory effects.[44]

The temperature dependence of the magnetization has been also examined for the selected samples after ZFC and FC with a small applied magnetic field of 50 Oe, respectively (Figure 4f). Owing to the presence of size distribution for the magnetic domains, the blocking temperature, T_B (at which superparamagnetism sets in), lies between T_{sat} (saturation temperature in the FC curve) and T_{irr} (irreversible temperature, at which the ZFC and FC curves coincide). The ZFC curve of the TP seeds exhibits an initial decrease up to 15 K, attributable to the soft spin-glasslike phase component, following which a maximum is reached, corresponding to $T_B \approx 96$ K for the harder inner FiM phase. Differently, the MIX sample, for which negligible soft phase has been

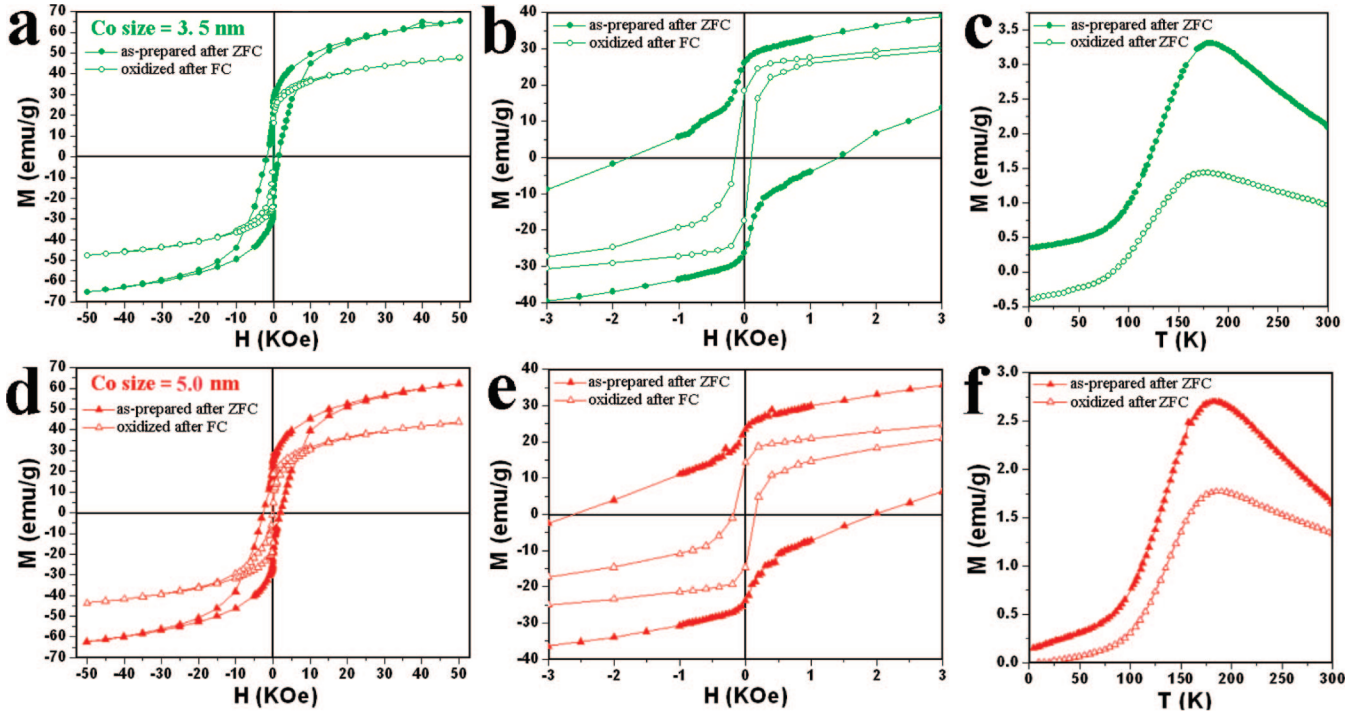

Figure 5. Effect of prolonged room-temperature air oxidation on the magnetic properties of dried HNCs synthesized from the same TP seeds (with mean arm diameter and length sizes of 5 ± 0.6 and 18 ± 2 nm, respectively) and carrying Co domains of about (a−c) 3.5 ± 0.4 nm and (d−f) 5.0 ± 0.7 nm. The panels report (a, d) full-view hysteresis loops recorded at 5 K for the as-prepared samples after ZFC and for the corresponding oxidized samples after FC with an applied field $H_{FC} = 5$ T, (b, e) low-field expanded view of the curves in panels a and d, respectively, and (c, f) temperature-dependent magnetization behavior after ZFC for the differently sized samples.

identified, does not in fact show any initial decay and is characterized by only slightly increased $T_B \approx 100$ K, in agreement with previous analysis of the corresponding hysteresis loop details. Notably, the HNC sample exhibits $T_B \approx 182$ K, a remarkably higher value that can hardly be accounted for by the Néel model, which in fact predicts T_B to scale up linearly with the magnetic volume, V_{NC}

$$T_B = K_a * V_{NC}/25K_B$$

where K_B is the Boltzmann constant and the anisotropy constant K_a comprises several terms.[38,39] One possible explanation could be that, as the two materials communicate through numerous inorganic junctions, proximity effects at the relevant connecting regions, e.g., related to spin uncompensation and/or pinning via exchange interaction, and/or to structural modifications, can induce a substantial increase in the overall anisotropy,[9−13,17,18,20] thereby enhancing the thermal stability of magnetization. The dominant role played by interface formation is further manifested by the negligible dependence of T_B for HNCs differing by the mean sizes of the Co domains (T_B lies between 178 and 184 K for Co sizes in the ∼3−6 nm range (cf. Table 2 and Figure S9 in the Supporting Information).

The origin of EB in the HNCs, as attributed above, can be understood on the basis of the following arguments. First, no loop shift has been detected for the MIX sample, which in fact discredits the hypothesis that EB in the HNCs is possibly related to Co_xO_y/Co junctions at the Co domain surfaces and/or to Co_xO_y/$CoFe_2O_4$/iron oxide interfaces at the TP/Co connecting points because of the operation of AFM-FM[9−16,18−20] or AFM-FiM coupling mechanisms,[9−16,21,22] respectively. Additionally, from these data it can be inferred that dipolar interparticle interactions are exceedingly weak to eventually induce efficient coupling in our composite powders of surfactant-protected NCs, in contrast to systems in which thermal treatment or mechanical stress is applied to promote alloying and/or coalescence,[22,38,40,41] or in which densely packed films of organic-free core/shell NCs are embedded in a matrix.[9,10,20]

Second, the fact that the TP seeds do not themselves exhibit EB phenomenology allows excluding any possible involvement of mere surface-related effects in nominally pure FiM nanomaterials, which would be related to the freezing of a metastable glasslike surface layer of spins and to its coupling to the inner ferrimagnetically ordered "core" phase.[9−14] It is also likely that for TP sizes, like those investigated here, the overall "bulk" anisotropy is large enough to overwhelm any surface effect. On the other hand, for such spinglass systems, a suppression in H_{EB} has commonly been observed at large H_{FC} values.[9−14]

Third, progressive elimination of the FM component of the HNCs upon deliberate oxidation of the dried samples under ambient conditions has a significant influence on the magnetic properties of the heterostructures. Upon air exposure Co starts to be converted to AFM Co_xO_y (mostly CoO) producing an oxide shell that develops until it approaches a limiting thickness at which the oxidation process practically arrests.[19,36] The Co volume fraction that is oxidized is proportionally larger for comparatively smaller metal domains (as estimated by the different TEM image contrast across the nanoparticles). The representative examples in Figure 5 address the cases of HNCs carrying differently sized

Co domains (~3.5 and ~5.0 nm), which could be extensively oxidized, attaining a relatively thick passivating oxide shell and consequent shrinking of the metallic core size (down to about 60% and 40% of the original value, respectively). The relevant data are summarized in Table 2. Besides leading to the expected reduction in magnetization,[19,36] the oxidation process results in almost complete suppression of the H_{EB} field recorded after FC (Figure 5, panels a, b, d, and e, in the respective situations). Concomitantly, a selective "softening" of the original hard phase component is achieved, as highlighted by the corresponding strong (up to 60%) reduction in H_C and by the more pronounced tendency of the loop toward reaching saturation. Both changes occur somewhat proportionally to the extent of oxidation (Table 2). It deserves also remarking that the EB signature vanishes steadily along the course of the oxidation period, which implies that the no EB coupling via AFM-FM interfaces eventually operates in our HNC system likely due to the poor structural quality of the CoO/Co interfaces that are produced upon mild air oxidation.[9−13,17,18,20] On the other hand, if large spin uncompensation at the Co/TP interfaces were involved in exchange coupling mechanism, EB should not be affected by the metal oxidation to any noticeable extent. Taken together, these observations actually indicate that EB in HNCs indeed arises from direct coupling of the FiM "core" phase of the iron oxide TPs to the FM phase of the attached Co domains, provided that the size of respective material domains and their relative ratio surpass some critical thresholds.

Interestingly, the ZFC temperature dependence of the magnetization of the oxidized samples (Figure 5c,f) displays only a minor drop in T_B of less than 10 K, regardless of the oxidation progress. On one side, these results further discredit any EB setting in at Co/CoO interfaces as a possible origin of increased anisotropy, since AFM-FM coupling should be instead expected to result in T_B increase.[18−20] On the other side, it can be inferred that FM-FiM exchange biasing does not here provide alone most of the extra anisotropy energy that would be responsible for thermal stabilization of the HNC magnetization, in contrast to that observed in other systems.[18−20] In this regard, it is plausible that the interplay of red−ox reactions (during the synthesis stage) and lattice-mismatch-induced strain at the Co/TP junction regions may generate a thin interfacial layer[35] with unique compositional and structural features that may unusually affect the overall anisotropy term.[9−28] More sophisticated characterization studies and theoretical modeling are currently underway to elucidate the structural and magnetic nature of the Co/TP interfaces, which appear to be the key for unraveling the specific mechanism that underlies FM-FiM exchange interactions.

In summary, we have described a seeded-growth approach to fabricate a new type of all-magnetic nanocrystal heterostructures, consisting of FiM iron oxide TPs functionalized with FM Co domains. Our synthesis technique enables high heterostructure yield by means of delayed delivery of selected surfactants to the reaction mixtures with respect to the heterogeneous nucleation stage. As a consequence of the efficient exchange coupling that is established between the relevant FiM and FM material sections, and of the interplay of anisotropy effects arising from the inherent tetrapod shape as well as from the newly attained chemical bonding at the involved heterointerfaces, the as-obtained HNCs exhibit a rich scenario of strongly modified magnetic properties, including higher saturation magnetization and coercitivity values, exchange bias, and increased blocking temperatures, all of which may find application in magnetic writing, storage, and reading. Such properties result in the interplay of exchange-coupling phenomenology, shape anisotropy (related to the iron oxide components), and interface anisotropy (due to the formation of iron oxide−Co bonding junctions). While extending the availability of wet chemically synthesized all-magnetic exchange-coupled HNCs beyond the conventional AFM-FM core/shell systems, our study suggests that development of appropriate methods for arranging multiple material domains in predetermined three-dimensional spatial arrangements via inorganic interfaces could lead to a more rational design of heterostructures potentially exploitable as active elements in future generations of magnetic recording devices.

Acknowledgment. This work was partially supported by the Italian Ministry of Research (contract no. RBIN048TSE), by the Spanish Ministry of Innovation (project FIS2008-06249), and by the Ministerio de Ciencia e Innovacion (project no. MAT2005-06024-C02-01).

Supporting Information Available: Experimental details on the synthesis procedure and on the characterization tools, example of size-selective separation of HNCs, quantitative phase analysis of XRD data, additional STEM-EDX analysis, monitoring of HNC growth, control synthesis experiments, additional magnetic data on HNCs with differently sized Co domains, and graphical procedure for determining the H_C and H_{EB} values for the soft/hard phases in the hysteresis loops. This material is available free of charge via the Internet at http://pubs.acs.org.

References

(1) Cozzoli, P. D.; Pellegrino, T.; Manna, L. *Chem. Soc. Rev.* **2006**, *35* (11), 1195–1208.
(2) Buonsanti, R.; Casavola, M.; Caputo, G.; Cozzoli, P. D. *Recent Pat. Nanotechnol.* **2007**, *1* (3), 224–232.
(3) Casavola, M.; Buonsanti, R.; Caputo, G.; Cozzoli, P. D. *Eur. J. Inorg. Chem.* **2008**, (6), 837–854.
(4) Caputo, G.; Buonsanti, R.; Casavola, M.; Cozzoli, P. D. Synthetic strategies to multi-material hybrid nanocrystals. In *Advanced Wet-Chemical Synthetic Approaches to Inorganic Nanostructures*; Cozzoli, P. D., Ed.; Transworld Research Network: Kerala, India, 2008; pp 407−453, ISBN 978-81-7895-361-8.
(5) Figuerola, A.; Fiore, A.; DiCorato, R.; Falqui, A.; Giannini, C.; Micotti, E.; Lascialfari, A.; Corti, M.; Cingolani, R.; Pellegrino, T.; Cozzoli, P. D.; Manna, L. *J. Am. Chem. Soc.* **2008**, *130* (4), 1477–1487.
(6) Chaubey, G. S.; Nandwana, V.; Poudyal, N.; Rong, C.-b.; Liu, J. P. *Chem. Mater.* **2008**, *20* (2), 475–478.
(7) Jun, Y.-w.; Choi, J.-s.; Cheon, J. *Chem. Commun.* **2007**, (12), 1203–1214.
(8) Jun, Y.-w.; Lee, J.-H.; Cheon, J. *Angew. Chem., Int. Ed.* **2008**, *47* (28), 5122–5135.
(9) Nogués, J.; Schuller, I. K. *J. Magn. Magn. Mater.* **1999**, *192* (2), 203–232.
(10) Nogués, J.; Sort, J.; Langlais, V.; Skumryev, V.; Suriñach, S.; Muñoz, J. S.; Baró, M. D. *Phys. Rep.* **2005**, *422* (3), 65–117.
(11) Li, K. B.; Wu, Y. H.; Guo, Z. B.; Zheng, Y. K.; Han, G. C.; Qiu, J. J.; Luo, P.; An, L. H.; Zhou, T. J. *J. Nanosci. Nanotechnol.* **2007**, *7* (1), 13–45.

(12) Radu, F.; Zabel, H. Exchange bias effect of ferro-/antiferromagnetic heterostructures. In *Magnetic Heterostructures*; Zabel, H., Bader, S. D., Eds.; Springer Berlin: Heidelberg, 2008; Vol. 227, pp 97−184.
(13) Iglesias, O.; Labarta, A.; Batlle, X. *J. Nanosci. Nanotechnol.* **2008**, *8* (6), 2761–2780.
(14) Iglesias, O.; Batlle, X.; Labarta, A. *J. Phys. D-Appl. Phys.* **2008**, *41* (13), 134010.
(15) Daly, B.; Arnold, Donna C.; Kulkarni, Jaideep S.; Kazakova, O.; Shaw, Matthew T.; Nikitenko, S.; Erts, D.; Morris, Michael A.; Holmes, Justin D. *Small* **2006**, *2* (11), 1299–1307.
(16) Kazakova, O.; Daly, B.; Holmes, J. D. *Phys. Rev. B* **2006**, *74* (18), 184413.
(17) Liu, W.; Zhong, W.; Du, Y. W. *J. Nanosci. Nanotechnol.* **2008**, *8* (6), 2781–2792.
(18) Nogues, J.; Skumryev, V.; Sort, J.; Stoyanov, S.; Givord, D. *Phys. Rev. Lett.* **2006**, *97* (15), 157203.
(19) Tracy, J. B.; Weiss, D. N.; Dinega, D. P.; Bawendi, M. G. *Phys. Rev. B* **2005**, *72* (6), 064404.
(20) Skumryevù, V.; Stoyanov, S.; Zhang, Y.; Hadjipanayis, G.; Givord, D.; Nogués, J. *Nature* **2003**, *423*, 850–853.
(21) van der Zaag, P. J.; Ball, A. R.; Feiner, L. F.; Wolf, R. M.; van der Heijde., P. A. A. *J. Appl. Phys.* **1996**, *79* (8), 5103–5105.
(22) Frandsen, C.; Ostenfeld, C. W.; Xu, M.; Jacobsen, C. S.; Keller, L.; Lefmann, K.; Mørup, S. *Phys. Rev. B* **2004**, *70* (13), 134416.
(23) Tamari, K.; Doi, T.; Horiishi, N. *Appl. Phys. Lett.* **1993**, *63* (23), 3227–3229.
(24) Yamamoto, S.; Andou, T.; Kurisu, H.; Matsuura, M.; Doi, T.; Tamari, K. *J. Appl. Phys.* **1996**, *79* (8), 4884–4886.
(25) Koujima, J.; Nakata, K.; Ando, T.; Shimomai, K.; Doi, T.; Sugiyama, M.; Cromwell, E. F. *IEEE Trans. Magn.* **2003**, *39* (4), 1936–1941.
(26) Masala, O.; Seshadri, R *J. Am. Chem. Soc.* **2005**, *127* (26), 9354–9355.
(27) Si, P. Z.; Li, D.; Lee, J. W.; Choi, C. J.; Zhang, Z. D.; Geng, D. Y.; Bruck, E. *Appl. Phys. Lett.* **2005**, *87* (13), 133122.
(28) Salazar-Alvarez, G.; Sort, J.; Surinach, S.; Baro, M. D.; Nogues, J. *J. Am. Chem. Soc.* **2007**, *129* (29), 9102–9108.
(29) Cozzoli, P. D.; Snoeck, E.; Garcia, M. A.; Giannini, C.; Guagliardi, A.; Cervellino, A.; Gozzo, F.; Hernando, A.; Achterhold, K.; Ciobanu, N.; Parak, F. G.; Cingolani, R.; Manna, L. *Nano Lett.* **2006**, *6* (9), 1966–1972.
(30) Puntes, V. F.; Krishnan, K. M.; Alivisatos, A. P. *Science* **2001**, *291* (5511), 2115–2117.
(31) Park, J.-I.; Kang, N.-J.; Jun, Y.-W.; Oh, S. J.; Ri, H.-C.; Cheon, J. *ChemPhysChem* **2002**, *3* (6), 543–547.
(32) Note that crystal shape anisotropy cannot be appreciated from inhomogeneous peak width due to intrinsic limits of the instrumental resolution function (see experimental details in the Supporting Information).
(33) Altomare, A.; Burla, M. C.; Giacovazzo, C.; Guagliardi, A.; Moliterni, A. G. G.; Polidori, G.; Rizzi, R. *J. Appl. Crystallogr.* **2001**, *34*, 392–397.
(34) Puntes, V. F.; Zanchet, D.; Erdonmez, C. K.; Alivisato, A. D. *J. Am. Chem. Soc.* **2002**, *124* (43), 12874–12880.
(35) (a) Christian, P.; Laurens, K. V.; Rudolf, D.; Rene, F. *J. Appl. Phys.* **2002**, *91* (3), 1251–1255. (b) Bezencenet, O.; Barbier, A.; Ohresser, P.; Belkhou, R.; Stanescu, S.; Owens, J.; Guittet, M. J. *Surf. Sci.* **2007**, *601* (18), 4321–4325. (c) Regan, T. J.; Ohldag, H.; Stamm, C.; Nolting, F.; Lüning, J.; Stöhr, J.; White, R. L. *Phys. Rev. B* **2001**, *64* (21), 214422. (d) Sani, R.; Beitollahi, A. *J. Non-Cryst. Solids* **2008**, *354* (40−41), 4635–4643.
(36) Casavola, M.; Grillo, V.; Carlino, E.; Giannini, C.; Gozzo, F.; Fernandez Pinel, E.; Garcia, M. A.; Manna, L.; Cingolani, R.; Cozzoli, P. D. *Nano Lett.* **2007**, *7* (5), 1386–1395.
(37) Wetz, F.; Soulantica, K.; Falqui, A.; Respaud, M.; Snoeck, E.; Chaudret, B. *Angew. Chem., Int. Ed.* **2007**, *46* (37), 7079–7081.
(38) *Surface Effects in Magnetic Nanoparticle*; Fiorani, D., Ed.; Springer: New York, 2005.
(39) Batlle, X.; Labarta, A. *J. Phys. D: Appl. Phys.* **2002**, *35* (6), R15–R42.
(40) Frandsen, C.; Mørup, S. *J. Magn. Magn. Mater.* **2003**, *266* (1−2), 36–48.
(41) Liu, X. H.; Cui, W. B.; Lv, X. K.; Liu, W.; Zhao, X. G.; Li, D.; Zhang, Z. D. *J. Appl. Phys.* **2008**, *103* (10), 103906.
(42) Under the assumption that M_S^{5K} of the pure TPs is preserved in their mixtures with Co NCs, on the basis of sample composition the magnetization contribution from the polycrystalline Co component can be roughly estimated to be of about 30 emu/g, which is consistent with literature data.
(43) Ziese, M.; Höhne, R.; Bollero, A.; Semmelhack, H. C.; Esquinazi, P.; Zimmer, K. *Eur. Phys. J. B* **2005**, *45* (2), 223–230.
(44) (a) Gökemeijer, N. J.; Cai, J. W.; Chien, C. L. *Phys. Rev. B* **1999**, *60* (5), 3033. (b) Li, Y. F.; Yu, R. H.; Xiao, J. Q.; Dimitrov, D. V. *J. Appl. Phys.* **2000**, *87* (9), 4951–4953. (c) Wen, G. H.; Zheng, R. K.; Fung, K. K.; Zhang, X. X. *J. Magn. Magn. Mater.* **2004**, *270* (3), 407–412.

NL803151N